# An Isc-Type Extremely Thermostable [2Fe−2S] Ferredoxin from *Aquifex aeolicus*. Biochemical, Spectroscopic, and Unfolding Studies†

Géraldine Mitou,‡ Catherine Higgins,§ Pernilla Wittung-Stafshede,§ Richard C. Conover,|| Archer D. Smith,|| Michael K. Johnson,|| Jacques Gaillard,⊥ Audria Stubna,# Eckard Münck,# and Jacques Meyer*,‡

*Département de Réponse et Dynamique Cellulaires, CEA-Grenoble, 38054 Grenoble, France, Chemistry Department, Tulane University, New Orleans, Louisiana 70118, Department of Chemistry and Center for Metalloenzyme Studies, University of Georgia, Athens, Georgia 30602, Département de Recherche Fondamentale sur la Matière Condensée, CEA-Grenoble, 38054 Grenoble, France, and Department of Chemistry, Carnegie Mellon University, Pittsburgh, Pennsylvania 15213*

*Received November 5, 2002; Revised Manuscript Received December 3, 2002*

ABSTRACT: Analysis of the genome of the hyperthermophilic bacterium *Aquifex aeolicus* has revealed the presence of a previously undetected gene potentially encoding a plant- and mammalian-type [2Fe−2S] ferredoxin. Expression of that gene in *Escherichia coli* has yielded a novel thermostable [2Fe−2S] ferredoxin (designated ferredoxin 5) whose sequence is most similar to those of ferredoxins involved in the assembly of iron−sulfur clusters (Isc-Fd). It nevertheless differs from the latter proteins by having deletions near its N- and C-termini, and no cysteine residues other than those involved in [2Fe−2S] cluster coordination. Resonance Raman, low-temperature MCD and EPR studies show close spectral similarities between ferredoxin 5 and the Isc-Fd from *Azotobacter vinelandii*. Mössbauer spectra of the reduced protein were analyzed with an $S = {}^1/_2$ spin Hamiltonian and interpreted in the framework of the ligand field model proposed by Bertrand and Gayda. The redox potential of *A. aeolicus* ferredoxin 5 (−390 mV) is in keeping with its relatedness to Isc-Fd. Unfolding experiments showed that *A. aeolicus* ferredoxin 5 is highly thermostable ($T_m = 106$ °C at pH 7), despite being devoid of features (e.g., high content of charged residues) usually associated with extreme thermal stability. Searches for genes potentially encoding plant-type [2Fe−2S] ferredoxins have been performed on the sequenced genomes of hyperthermophilic organisms. None other than the two proteins from *A. aeolicus* were retrieved, indicating that this otherwise widely distributed group of proteins is barely represented among hyperthermophiles.

Ferredoxins (Fds)[1] known as "plant- and mammalian-type Fd" contain [2Fe−2S] clusters (*1*−*5*) and are widely distributed among living organisms. That monophyletic family of proteins is composed of two main subgroups. The first of these consists of Fds transferring electrons from photosystem I to several Fd-dependent enzymes in plants, algae, and cyanobacteria (*3*). Fds of the second subgroup participate in electron-transfer chains linked to hydroxylation reactions, in mammals (e.g., adrenodoxin (Adx)) as well as in a variety of other organisms, including bacteria (e.g., putidaredoxin (*4*)).

Novel functions of [2Fe−2S] Fds have recently been unveiled. Thus, some of them are involved in the assembly of iron−sulfur clusters in vivo (*6*−*8*) and are related to Adx (hence the name Yah1p—for yeast adrenodoxin homologue—given to one member of this group (*9*)). Other [2Fe−2S] Fds have been shown to be very specific reactivators of oxygen-inactivated dioxygenases (*10*). These functional subclasses of plant- and mammalian-type [2Fe−2S] Fds are, to some extent at least, identifiable by sequence idiosyncrasies which are reflected in the presence of separate branches in dendrograms derived from sequence alignments (*11*−*12*).

These recent findings suggest that the structure, function, and distribution of [2Fe−2S] Fds remain to be fully explored. Indeed, until very recently, [2Fe−2S] plant- and mammalian-type Fds were unknown in hyperthermophilic organisms. The single exception known to date, Fd1 from *Aquifex aeolicus* (*11*, *13*), prompted us to search genomes of hyperthermophiles for such Fds. This inspection has confirmed, surprisingly, that Archaea other than halophiles, and likewise hyperthermophilic bacteria of the genus *Thermotoga*, appear to be devoid of [2Fe−2S] Fd. Nevertheless, a heretofore nonannotated sequence potentially encoding a [2Fe−2S] Fd has been detected in the genome of *A. aeolicus*. This open

† This research was supported by the Université J. Fourier Grenoble (EA 2943, J.M.), the National Institutes of Health (Grants GM59663 to P.W.-S. and GM62524 to M.K.J.), and the National Science Foundation (Grant MCD-9416224 to E.M.). P.W.-S. is an Alfred P. Sloan Research Fellow. C. Higgins is supported by a fellowship from the Louisiana Board of Regents.

* To whom correspondence should be addressed. Tel: (33) 4 38 78 44 23. FAX: (33) 4 38 78 98 08. E-mail: jacques.meyer@cea.fr.

‡ Département de Réponse et Dynamique Cellulaires, CEA-Grenoble.

§ Tulane University.

|| University of Georgia.

⊥ Département de Recherche Fondamentale sur la Matière Condensée, CEA-Grenoble.

# Carnegie Mellon University.

[1] Abbreviations: *Aae*, *Aquifex aeolicus*; *Av*, *Azotobacter vinelandii*; Adx, adrenodoxin; CD, circular dichroism; efg, electric field gradient; ENDOR, electron−nuclear double resonance; EPR, electron paramagnetic resonance; Fd(s), ferredoxin(s); GuHCl, guanidine hydrochloride; Isc, iron−sulfur cluster assembly; VTMCD, variable temperature magnetic circular dichroism; SDS, sodium dodecyl sulfate; PAGE, polyacrylamide electrophoresis; PCR, polymerase chain reaction; Pdx, putidaredoxin; RR, resonance Raman; WT, wild type.

10.1021/bi027116n CCC: $25.00 
Published on Web 01/15/2003

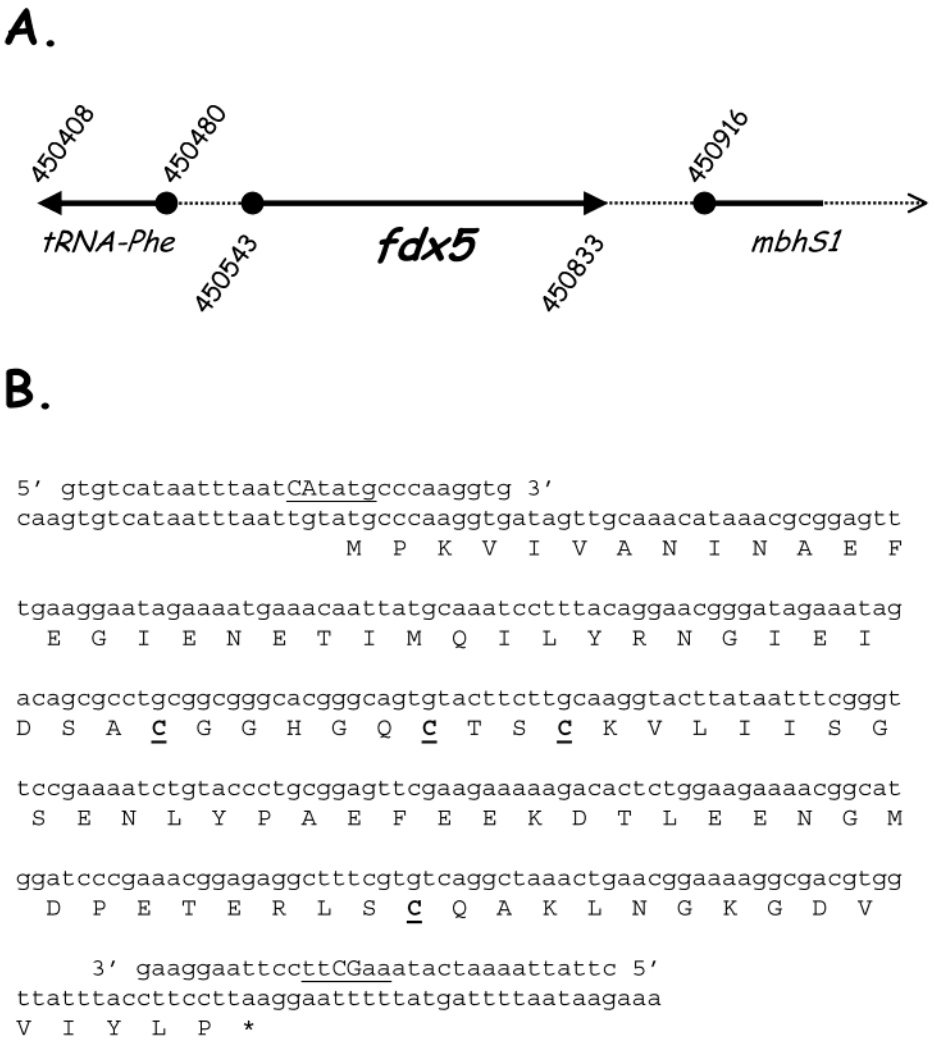


FIGURE 1: (A) Position (base numbers indicated) in the *A. aeolicus* genome (*15*) of the newly detected *fdx5* gene. (B) Gene and protein sequence of Fd5. Also shown are the primers used to lift the gene from genomic DNA by PCR (see text).

reading frame has been cloned, overexpressed in *Escherichia coli*, and shown to encode an adrenodoxin-like highly thermostable [2Fe−2S] Fd whose properties are described below.

## MATERIALS AND METHODS

Enzymes were purchased from Roche Applied Science (Meylan, France). Oligonucleotides and culture media were from Life Technologies (Cergy-Pontoise, France). Guanidine hydrochloride (GuHCl), of the highest purity, was purchased from Sigma. Polymerase chain reactions (PCR) were run on a Perkin-Elmer 2400 machine. Plasmid DNA was purified with the EasyPrep kit (Pharmacia). DNA sequencing was performed by Genome Express (Meylan, France).

*Gene Cloning and Protein Purification.* All common DNA manipulations were as described (*14*). The novel Fd-encoding gene was lifted from *A. aeolicus* genomic DNA (gift from Dr. R. Huber, University of Regensburg, Germany) by PCR using the following primers (see Results and Figure 1). The N-terminal primer hybridized to the noncoding strand: 5′ gtgtcataatttaat*catATG*cccaaggtg 3′ (*Nde*I restriction site in italics, ATG start codon in upper case). The C-terminal primer hybridized to the coding strand: 5′ cttattaaaatcat-a*aagctt*ccTTAaggaag 3′ (*Hin*dIII restriction site in italics, stop codon in upper case). After a DNA denaturation step of 5 min at 94 °C, *Pwo* DNA polymerase and the deoxynucleotide mix were added, and 25 cycles of amplification (30 s at 94 °C, 30 s at 50 °C, 2 min at 72 °C) were performed, followed by a 7 min elongation step. The amplified DNA fragment was extracted with phenol/chloroform, precipitated with ethanol, digested with *Hin*dIII and *Nde*I, purified by electrophoresis through a low-melting agarose gel, and ligated into the pT7−7 vector (*16*) digested with the same restriction enzymes. The ligation mixture was used to transform *Escherichia coli* DH5α cells. Clones containing the Fd1-encoding gene were sequenced and found to match perfectly the corresponding part of the *A. aeolicus* genome sequence (*15*). The Fd-encoding gene was expressed in *E. coli* K38 cells using the pT7−7 and pGP1−2 double plasmid system (*16*) as described previously for the [2Fe−2S] *Clostridium pasteurianum* Fd (*17*). Cells from a 10 L culture in minimal medium (M9 from Life Technologies, complemented with 0.2% glucose, 1 mM $MgSO_4$, 25 $\mu$M Fe−citrate, 0.5 mg/L vitamin B1, 100 mg/L ampicillin, 50 mg/L kanamycin) were resuspended in 250 mL of Tris-HCl 50 mM, pH 8.0, disrupted by sonication (3 × 1 min at 300 W), and centrifuged 30 min at 35 000*g*. The supernatant was heated to 65 °C for 10 min, kept at 0 °C for another 10 min,

and centrifuged (35 000*g*, 30 min) to remove the denatured *E. coli* proteins. The dark red supernatant was loaded on a 2 × 7 cm DE-52 (Whatman) column equilibrated with Tris-HCl 50 mM, pH 8.0. From this step on, the purification was carried out under argon. The DE−52 column was washed with Tris-HCl 50 mM, pH 8.0, containing stepwise incremented concentrations of NaCl (0.05, 0.1, 0.2, 0.25, and 0.3 M). The Fd was eluted with 0.3 M NaCl, concentrated in an Amicon cell fitted with a PM10 membrane, and loaded on a 1.5 × 100 cm Superdex-75 (Pharmacia) column equilibrated with Tris-HCl 20 mM, pH 8.0, NaCl 0.2 M. The last purification step was an HPLC chromatography on a PL-SAX (Polymer Labs) anion-exchange column developed with a 0−0.4 M NaCl gradient in Tris-HCl 0.01M, pH 8.0. The purified Fd displayed the characteristic reddish brown color of [2Fe−2S] proteins. Its purification was monitored by SDS−PAGE electrophoresis (not shown) and by the increase of the A420/A280 ratio (see Results).

*Azotobacter vinelandii* FdIV (*Av* Isc-Fd) was overexpressed in *E. coli* and purified to homogeneity according to published procedures (*6*).

*Analytical Methods*. N-terminal protein sequencing, amino acid analyses, and mass spectrometry were performed as described (*18*). Iron was assayed by a colorimetric method (*19*).

*Redox Potentials*. Redox potentials were measured in an oxygen-free (2 ppm) glovebox at 20 °C by reductive and oxidative titrations with dithionite and ferricyanide, respectively, as described (*20*, *21*). The reaction medium (2.3 mL) contained 50 mM Tris-HCl, pH 8.0, 0.2 M NaCl, 0.08 mM Fd, and the mediators indigo carmine (Sigma), safranine T (Fluka), benzyl viologen, and methyl viologen (Serva), each at a concentration of 1.5 $\mu$M. UV−visible absorption spectra were recorded in the 350−800 nm range, and the absorbance at 460 nm, where the contribution of the mediators is negligible, was used for the calculations. The potential was measured between the platinum electrode and the Ag/AgCl reference electrode of a combined electrode.

*Spectroscopic Methods*. UV−visible absorption spectra were recorded on Hewlett-Packard 8452 or 8453 diode-array spectrophotometers. EPR spectra were recorded using an X-band Bruker ESP-300E EPR spectrometer equipped with a dual-mode ER-4116 cavity and an Oxford Instruments ESR-9 flow cryostat. Frequencies were measured with either a Systron-Donner 6054B frequency counter or Hewlett-Packard 5350B microwave frequency counter, and the magnetic field was calibrated with a Bruker ER035M gaussmeter. Spin quantitations were carried out under nonsaturating conditions using 1mM Cu(II)EDTA as the standard. Spectral simulations were carried out using the Bruker Simfonia software package. VTMCD spectra were recorded using an Oxford Instruments Spectromag 4000 split-coil superconducting magnet (1.5−300 K and 0−7 T) mated to a Jasco J-720 spectropolarimeter. The samples used for VTMCD contained 60% (v/v) ethylene glycol in order to form an optically transparent glass on freezing. The experimental protocols used in VTMCD studies, namely, accurate temperature and magnetic field measurements, anaerobic sample handling, and assessment of residual strain in the frozen samples, have been described in detail elsewhere (*22*, *23*). Resonance Raman (RR) spectra were recorded using an Instruments SA Ramanor U1000 spectrometer fitted with a cooled RCA 31034 photomultiplier tube with a 90° scattering geometry. Spectra were recorded digitally using photon-counting electronics. Multiple scans (up to 50) were collected and averaged in order to increase the signal-to-noise ratio. Band positions were calibrated using the excitation frequency and a $CCl_4$ standard and are accurate to within $\pm 1$ cm$^{-1}$. Lines from Coherent Innova 100 10-W argon ion laser were used in this work and plasma lines were removed using a Pellin-Broca prism premonochromator. Scattering was collected from the surface of a frozen 10 $\mu$L drop of sample using a custom designed anaerobic sample cell (*24*) attached to the coldfinger of an Air Products Displex Model CSA-202E closed cycle refrigerator. The Mössbauer spectra were collected on a constant acceleration spectrometer, using two cryostats that allowed studies in applied fields up to 8.0 T between 1.5 K and room temperature. Isomer shifts are quoted relative to Fe metal at 298 K. Spectral simulations were generated with the WMOSS software package (WEB Research, Edina, MN). Cultures for the preparation of $^{57}$Fe-enriched Fd were as described (*13*).

*Chemically Induced Unfolding*. The available pH range for integrity of the Fd (in buffer, 20 °C) was tested using the following buffers: pH 12.4, KCl−NaOH; pH 11, $NaHCO_3$−NaOH; pH 10, glycine-OH; pH 7, phosphate; pH 4, citric acid-$NaH_2PO_4$; pH 2.5, glycine-HCl; pH 1.57 and 1.25, KCl−HCl. After 2 h of incubation at each pH, far-UV CD (200−300 nm) and visible absorption (300−700 nm) spectra were collected. GuHCl was used to promote Fd unfolding at 20 °C at pH values between 2.5 and 11. Titrations were performed with 10−20 $\mu$M Fd. Samples were incubated for various lengths of time (2, 12, 24, 48 h) before spectroscopic measurements. Unfolding was probed by far-UV CD (200−300 nm) on a JASCO-820 instrument, by visible absorption (300−700 nm) on a Cary-50 spectrophotometer, and by tyrosine emission (300−450 nm, excitation at 280 nm) on a Varian Eclipse instrument. The transition midpoint ($[GuHCl]_{1/2}$) at each solution condition (pH, incubation time) was obtained by direct inspection of the data.

*Thermally Induced Unfolding.* Thermally induced unfolding of Fd was monitored by visible absorption at 418 nm in various pH/GuHCl conditions. The absorption signal from ~15 $\mu$M Fd was recorded, one data point collected per second, with 0.5, 0.25, and 0.125 deg/min scan rates from 20 to 95 °C. The thermal reactions were monitored on a Cary-100 spectrophotometer. In the end, the temperature was decreased to 20 °C and a spectrum recorded to check for refolding. The thermal midpoint ($T_m$) at each GuHCl concentration was calculated by direct inspection of the transition. First, $T_m$ values at various GuHCl concentrations were extrapolated to yield $T_m$ in 0 M GuHCl for each scan rate. Next, these $T_m$ values were extrapolated to infinite scan rate.

## RESULTS AND DISCUSSION

*Cloning*. Fd-encoding genes are small enough (180−300 bases) to be occasionally overlooked in genome sequence annotations. In our search of as yet unidentified [2Fe−2S] Fds, we therefore implemented published annotations, as well as the TBLASTN search software (*25*) that has the potential to detect protein-encoding segments in any DNA sequence.

Several [2Fe−2S] Fd sequences were used as baits, in particular those of Fds involved in Fe−S cluster assembly in vivo. In one such run, a nonannotated segment of the *A. aeolicus* genome was retrieved with a high score. This segment, which has the potential to encode a full-length [2Fe−2S] Fd, is located between genes encoding Phe-tRNA and a small subunit NiFe hydrogenase (Figure 1). According to the surrounding sequence, this putative Fd-encoding gene would be monocistronic. The Fd-encoding ability of that gene was demonstrated by cloning, expression in *E. coli* (see Methods), and isolation of the expected [2Fe−2S] Fd. Since altogether four Fd-encoding genes had been identified (and numbered 1−4) in the genome of *A. aeolicus* (*15*), we have named ferredoxin 5 (Fd5) the gene product obtained and described in this report.

*Purification*. The thermostability of *Aae* Fd5 (see below) suggested a thermal treatment of the *E. coli* cell extracts, as described for *A. aeolicus* Fd4 (*26*) and Fd1 (*11*), to remove most of the *E. coli* proteins. As anticipated from the acidity of *Aae* Fd5 (calculated pI = 4.2), anion-exchange chromatography proved to be a very efficient purification step. The purity of Fd5, as monitored by SDS−PAGE (not shown) and UV−visible absorption spectroscopy, was satisfactory after the gel filtration in most cases. Otherwise, a final anion-exchange HPLC step was performed.

*Biochemical Characterization.* Automated Edman degradation of *Aae* Fd5 confirmed the N-terminus as predicted from the gene sequence and showed that the N-terminal methionine was removed posttranslationally. ESI-MS spectra confirmed the mass of the apoprotein and the presence of a [2Fe−2S] cluster. Iron assays and amino acid analyses yielded an iron content of 2.2 ± 0.2 Fe atoms per molecule of Fd5. An actual number of two Fe atoms per protein molecule is indicated by the Mössbauer spectra of the oxidized protein (see below), which indicate that no iron other than that of the diferric site is present. On the basis of the Fe content, the extinction coefficient of the [2Fe−2S] cluster at 415 nm is 9400 $M^{-1}$ $cm^{-1}$.

*Amino Acid Sequence Comparisons*. The amino acid sequence of *Aae* Fd5 consists of 95 residues and is clearly related to those of plant- and mammalian-type Fds. Unlike the previously characterized *Aae* Fd1 (*11*), Fd5 does not possess the additional cysteine residues that would allow formation of a disulfide bridge. It also differs from Fd1 by not having the unusually high content in charged residues (Glu and Lys in particular) that characterizes hyperthermophilic proteins (*27*). The sequence of *Aae* Fd5 has been aligned with those of representative members of the plant- and mammalian-type Fds, as previously done with *Aae* Fd1 (*11*). The alignment (see Supporting Information) is consistent with recently published ones (*4*, *11*, *12*). A dendrogram (Figure 2) derived from the alignment highlights the various subgroups of the plant- and mammalian-type Fds (*11*). *Aae* Fd5 is related to the bacterial Isc-Fds (*6*−*8*), although somewhat on the margins of that group (Figure 2). Indeed, comparisons of *Aae* Fd5 with Isc-Fds (see Supporting Information) reveal noteworthy discrepancies: while Isc-Fd sequences (excluding *Aae* Fd5) are highly conserved (over 50% identities), the inclusion of *Aae* Fd5 in the alignment lowers the identities to 25%. *Aae* Fd5 differs from the other sequences by deletions near its N- and C-terminus and by a lower content of cysteine residues.

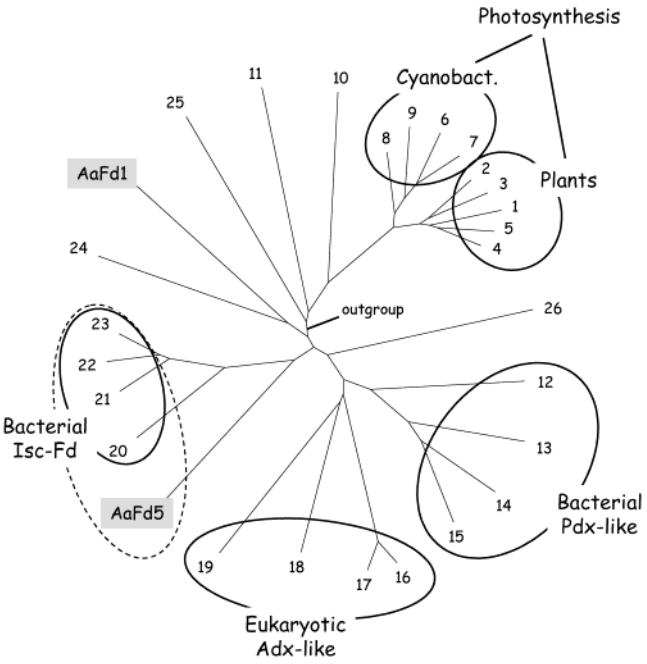


FIGURE 2: Graphical representation of the similarities between the sequences of various [2Fe−2S] ferredoxins. Sequences are designated by numbers as indicated hereafter (Genbank protein accessions in parentheses). 1, *Spinacia oleracea* (spinach) FdI (FESP1); 2, *Petroselinum crispum* (parsley) Fd (A61291); 3, *Zea mays* (maize) Fd2 (T01170); 4, *Alocasia macrorrhizos* FdA (S28198); 5, *Datura stramonium* Fd (P81454) 6, *Anabaena* strain PCC7119 Fd (P06543); 7, *Spirulina platensis* Fd (FESGAL); 8, *Synechocystis* strain PCC6803 Fd (FEYB6); 9, *Synechococcus* sp. Fd (FEYCT); 10, *Haloarcula marismortui* (FEHSX); 11, *Pseudomonas putida* XylT (S16193); 12, *Pseudomonas putida* putidaredoxin (PXPSEP); 13, *Rhodobacter capsulatus* FdVI (S45612); 14, *Caulobacter crescentus* FdII (P37098); 15, *Mesorhizobium loti* Fd (BAB48308); 16, *Bos taurus* (bovine) adrenodoxin (BAA00363); 17, *Homo sapiens* (human) adrenodoxin (AXHU); 18, *Saccharomyces cerevisiae* Yah1p (S0006173); 19, *Drosophila melanogaster* Hsp-Fd (CAB55551); 20, *Buchnera* sp. APS Fd (BAB13290); 21, *Escherichia coli* Isc-Fd (P25528); 22, *Azotobacter vinelandii* Isc-Fd (FdIV) (T44286); 23, *Pseudomonas aeruginosa* PA01 Isc-Fd (NP_252498); 24, *R. capsulatus* FdIV (P16022); 25, *R. capsulatus* FdV (P37097); 26, *Trichomonas vaginalis* Fd (A36003) (*28*); Aa Fd1, *A. aeolicus* Fd1 (O67065); Aa Fd5, *A. aeolicus* Fd5. The outgroup comprises two *C. pasteurianum* proteins unrelated to each other and to the Fds shown here: rubredoxin (RUCLEP) and [2Fe−2S] Fd (FECL2P). The dendrogram generated by CLUSTALW from sequence alignments (*29*) was visualized using TreeView (*30*).

*Spectroscopy*. The UV−visible absorption spectrum of as-isolated *Aae* Fd5 exhibits bands at 460, 415, and 342 nm (Figure 3), characteristic of $[2Fe-2S]^{2+}$ clusters. The purest Fd5 fractions had an $A_{415}/A_{276}$ absorbance ratio of 0.70. Upon reduction with dithionite to the $[2Fe-2S]^{+}$ level, the absorbance decreased over the whole visible range, but a broad band remained observable at 545 nm (Figure 3). The spectra of both oxidation states are nearly identical to those reported for Isc-Fd from *E. coli* (*31*) and *A. vinelandii* (*6*).

Resonance Raman spectra in the Fe−S stretching region provide a sensitive structural probe for the structure and environment of biological $[2Fe-2S]^{2+}$ clusters and distinctive spectra are observed for the major subclasses of plant-type and mammalian-type [2Fe−2S] Fds (*32*−*35*). As shown in Figure 4, the RR spectrum of as-isolated *Aae* Fd5 is very similar to that of the archetypal Isc-Fd from *A. vinelandii*, in terms of both the relative intensities and frequencies of discrete bands. The spectra shown were obtained with 458

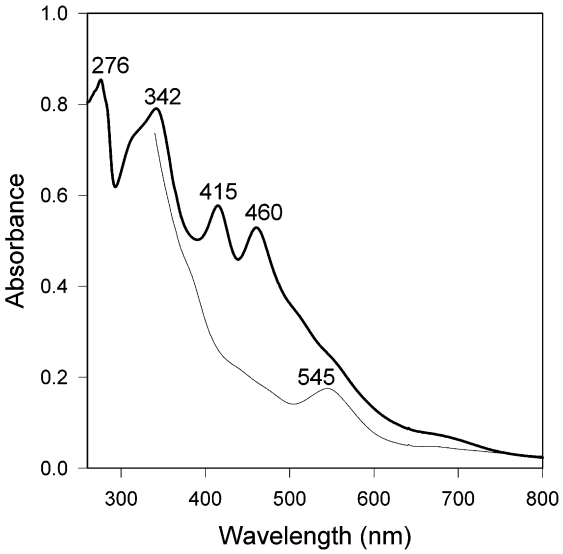


FIGURE 3: UV−visible absorption spectra of oxidized (thick line) and dithionite-reduced (thin line) *A. aeolicus* Fd5. The optical cell (path length: 1 mm) containing 0.25 mL of a 6 mg/mL solution of Fd5 (solvent: NaCl 0.2M, TrisHCl 20 mM, pH 8) was sealed with a rubber septum and flushed with argon. After recording the spectrum of the oxidized protein, 1 $\mu$L aliquots of a 20 mM dithionite solution were injected until no further decrease of the absorbance occurred in the 400−500 nm region. The spectrum of the reduced protein was then recorded.

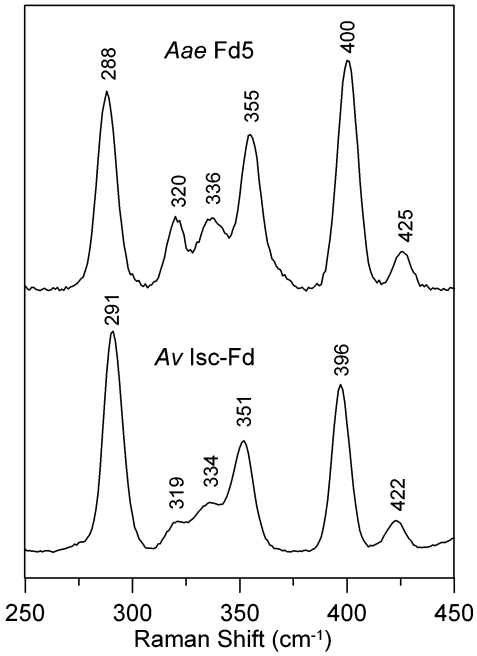


FIGURE 4: Comparison of the resonance Raman spectra of the $[2Fe-2S]^{2+}$ centers in *Aae* Fd5 and *Av* Isc-Fd. The spectra were recorded with 457.9 nm excitation using frozen droplets of concentrated samples (~3 mM) maintained at 17 K. The spectra are the sum of 50 scans with each scan involving photon counting for 1 s every 1 $cm^{-1}$ increment and 6 $cm^{-1}$ spectral resolution. Bands originating from the frozen buffer solution have been subtracted from both spectra.

nm excitation, but the same conclusion is applicable to data collected using 488 and 514 nm excitation wavelengths (data not shown). Moreover the spectra are very similar to those of mammalian- or hydroxylase-type [2Fe−2S] Fds typified by bovine (*34*) and human (*11*) adrenodoxin and by *Pseudomonas putida* putidaredoxin (*35*). The RR spectra of

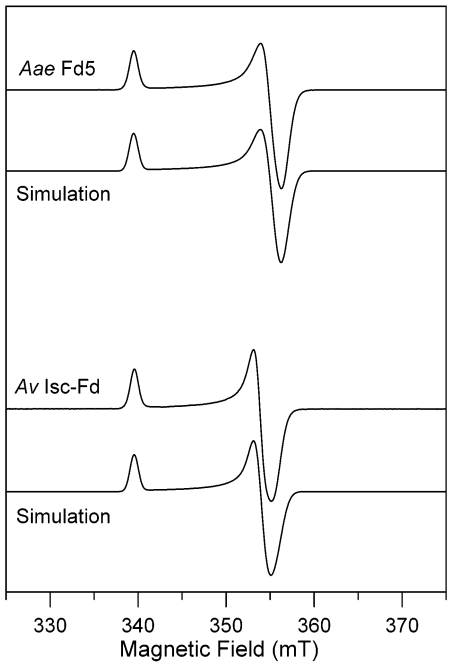


FIGURE 5: Comparison of the X-band EPR spectra of the $[2Fe-2S]^{+}$ centers in dithionite-reduced *Aae* Fd5 and *Av* Isc-Fd. The spectra were recorded at 35 K with a microwave power of 0.1 mW, modulation amplitude of 0.63 mT, and a microwave frequency of 9.60 GHz. The sample concentrations were 0.87 mM for *Aae* Fd5 and 0.38 mM for *Av* Isc-Fd, and the samples were in 20 mM Tris/HCl buffer, pH 8.0, with 0.1 M NaCl and 2 mM sodium dithionite and in 100 mM Tris/HCl buffer, pH 7.8, with 2 mM sodium dithionite for *Aae* Fd5 and *Av* Isc-Fd, respectively. The parameters for the simulated spectra were $g_{x,y,z} = 1.926, 1.931, 2.021$ and $l_{x,y,z} = 19.0, 19.0, 10.0$ G for *Aae* Fd5 and $g_{x,y,z} = 1.930, 1.939, 2.021$ and $l_{x,y,z} = 17.5, 13.0, 9.5$ G for *Av* Isc-Fd.

bovine Adx and *P. putida* Pdx have been rigorously assigned on the basis of $^{34}S/^{32}S$ isotope shifts, studies of synthetic analogue complexes, and normal-mode calculations (*33*−*35*). The spectra for *Aae* Fd5 and *Av* Isc-Fd can be assigned by direct analogy on the basis of the one-to-one correspondence of the individual bands.

EPR and VTMCD spectroscopies provide complementary approaches for investigating the electronic properties of $S = {}^1/_2$ $[2Fe-2S]^{+}$ clusters. EPR provides a detailed assessment of the ground state *g*-value anisotropy that is determined primarily by distortions from idealized tetrahedral symmetry at the valence-localized ferrous site (*36*−*38*). In contrast, the VTMCD spectrum in the visible region is dominated by sulfur-to-Fe(III) charge-transfer transitions (*35*, *39*). Both techniques have proven effective in distinguishing between mammalian- and plant-type $[2Fe-2S]^{+}$ centers in Fds (*35*, *39*).

The EPR spectrum of the $S = {}^1/_2$ $[2Fe-2S]^{+}$ center in dithionite-reduced *Aae* Fd5 displays a near-axial signal ($g = 2.021, 1.931, 1.926$) that is very similar to that observed for dithionite-reduced *Av* Isc-Fd ($g = 2.021, 1.939, 1.930$), see Figure 5, and both account for $1.0 \pm 0.2$ spins/molecule. Approximately axial $S = {}^1/_2$ EPR signals with $g_{||} \cong 2.02$ and $g_{\perp} \cong 1.94$ are a characteristic feature of the $[2Fe-2S]^{+}$ clusters in mammalian Adx-like, bacterial Pdx-like and bacterial Isc-Fd (*31*, *40*, *41*). In contrast the $[2Fe-2S]^{+}$ centers in plant-type [2Fe−2S] Fds exhibit rhombic $S = 1/2$ resonances with $g \cong 2.05, 1.96, 1.89$. The similarity between *Aae* Fd5 and Isc-Fds is underscored by the nearly identical

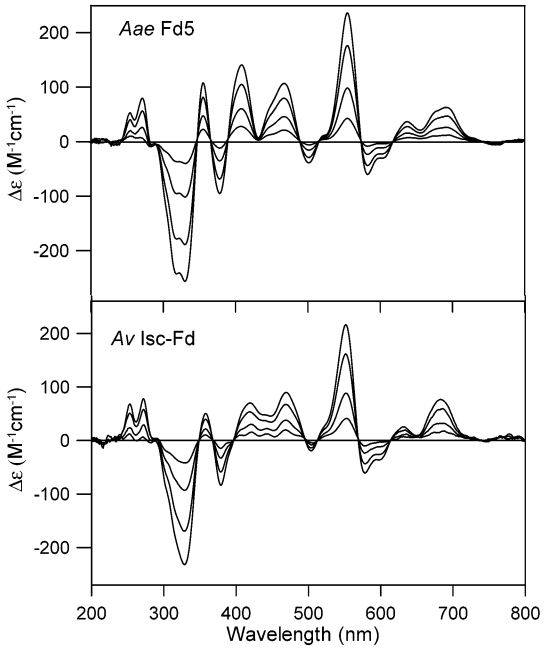


FIGURE 6: Comparison of the VTMCD spectra of the $[2Fe-2S]^+$ centers in dithionite-reduced *Aae* Fd5 and *Av* Isc-Fd. The spectra were recorded with an applied field of 6 T at 1.94, 4.22, 9.8, and 24.8 K for *Aae* Fd5 and at 1.97, 4.22, 10.2, and 23.8 K for *Av* Isc-Fd. All bands increase in intensity with decreasing temperature. The samples were the same as those described in Figure 5, except for the addition of 60% (v/v) ethylene glycol, and the final concentrations were 0.35 mM for *Aae* Fd5 and 0.15 mM for *Av* Isc-Fd.

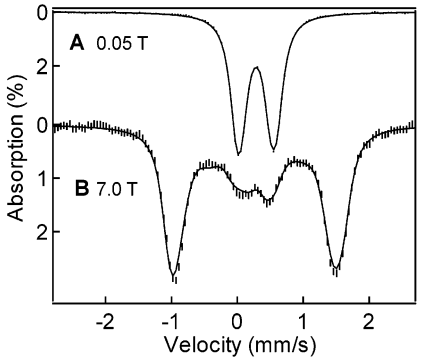


FIGURE 7: 4.2 K Mössbauer spectra of oxidized Fd5 recorded in 0.05 T (A) and 7.0 T (B) fields applied parallel to the $\gamma$-beam. The solid lines are theoretical spectra assuming two sites with $\Delta E_Q(1) = +0.62$ mm/s, $\eta(1) = 0.75$, $\delta(1) = 0.29$ mm/s and $\Delta E_Q(2) = +0.44$ mm/s, $\eta(2) = 0.75$, $\delta(2) = 0.28$ mm/s. For (B) diamagnetic sites were assumed.

relaxation properties of all these proteins at 12 K (data not shown). The conclusion that the electronic properties of the $[2Fe-2S]^+$ center in *Aae* Fd5 are most similar to those of bacterial Isc-type Fd such as *Av* Isc-Fd is further supported by the excited-state properties as revealed by VTMCD spectroscopy (Figure 6). The VTMCD spectra display a one-to-one correspondence of positive and negative bands throughout the UV/visible/near-IR region. Very similar VTMCD spectra have been reported for reduced bovine and human Adx (*11*, *39*) and *P. putida* Pdx (*35*).

Mössbauer spectra of oxidized Fd5 recorded at 4.2 K in 0.05 T (A) and 7.0 T (B) fields are shown in Figure 7. The 0.05 T spectrum is best fit with two subcomponents having $\Delta E_Q(1) = +0.62$ mm/s and $\delta(1) = 0.29$ mm/s, and $\Delta E_Q(2) = +0.44$ mm/s and $\delta(2) = 0.28$ mm/s. The spectrum of Figure 7B shows that the oxidized [2Fe−2S] cluster has a diamagnetic ground state, as expected. Spectral simulations yield the quoted signs for $\Delta E_Q$ as well as the asymmetry parameters for the electric field gradient (efg) tensors of the two sites, $\eta(1) = \eta(2) = 0.75$. It is possible to simulate the spectrum with a combination of different $\eta$ values as long as $\eta > 0.5$ for each site ($\eta = 0$ is for axial symmetry).

Figure 8 shows Mössbauer spectra of dithionite-reduced Fd5 recorded at 4.2 K in applied fields as indicated. Two samples have been studied, which could both be reduced to only ca. 75−80%. However, since the spectra of the oxidized protein are well understood, their contribution (20% of total Fe) could be removed from the spectra, as done in Figure 8A,B,D. The reduced samples contained also a high-spin ferrous component (4% of total Fe) with $\Delta E_Q \approx 3.0$ mm/s, $\delta \approx 1.3$ mm/s. This minor contaminant most likely results from cluster destruction upon reduction with dithionite, as it is not present in the spectra of Figure 7. We have removed its contribution from the spectra of Figure 8A,B, but not from the 7.0 T spectrum of Figure 8D. In the latter case, however, the applied field spreads its absorption over a wide velocity range and the presence of the contaminant does not significantly affect the analysis. Under the conditions of panels A and B the spectra of the oxidized Fd5 and the ferrous contaminant do not depend on the direction of the applied field, and thus their contributions cancel in the difference spectrum of Figure 8C.

We have analyzed the spectra of reduced Fd5 with the $S = {}^1/_2$ spin Hamiltonian

$$H = \beta \mathbf{S}\cdot\mathbf{g}\cdot\mathbf{B} + \sum_{i=1}^{2}\left\{\mathbf{S}\cdot\mathbf{A}(i)\cdot\mathbf{I}(i) - g_n\beta_n\mathbf{B}\cdot\mathbf{I}(i) + \frac{eQV_{\zeta\zeta}(i)}{12}[3\mathbf{I}_\zeta^2(i) - (15/4) + \eta(i)(\mathbf{I}_\xi^2(i) - \mathbf{I}_\eta^2(i))]\right\} \quad (1)$$

where all quantities have their conventional meanings. The efg tensor is commonly quoted in a coordinate frame for which its largest component is along the *z*-axis. In such a system (denoted $\xi$, $\eta$, $\zeta$ in eq 1), the sign of $\Delta E_Q$ reflects the sign of the largest efg component. The solid lines drawn through the spectra of Figure 9 are the result of simulations according to described procedures (*42*, *43*) yielding the parameters listed in Table 1. For the 7.0 T spectrum (Figure 8D), the contributions of the ferric and ferrous site are shown separately. The largest component of the efg-tensor, $V_{\zeta\zeta}$, is positive and directed along the *y*-axis of the **A**-tensor. The asymmetry parameter of the efg is $\eta = 0.4 \pm 0.2$, showing that the ferrous site is not axial.

The relaxation of the electronic spin of Fd5 is relatively fast above 200 K so that the ferrous site displays a quadrupole doublet (not shown). In contrast, because of its larger *A*-values, the ferric site experiences intermediate relaxation rates resulting in broad unresolved features at 200 K (not shown). From spectra measured at 200 and 230 K (not shown), we obtained a temperature-independent $\Delta E_Q = 2.9$ mm/s and $\delta = 0.58$ mm/s (at 200 K) for the ferrous site. With this information and correcting for the second-order Doppler shift, we obtained $\Delta E_Q$ and $\delta$ at 4.2 K.

Bertrand and Gayda (*44*) have proposed a ligand field model for the ferrous site of [2Fe−2S] ferredoxins that

Table 1: Hyperfine Parameters of Reduced *Aae* Fd5[a]

| | $Fe^{3+}$ | | | | | | $Fe^{2+}$ | | | | | |
|---|---|---|---|---|---|---|---|---|---|---|---|---|
| | $\Delta E_Q$ (mm/s) | $\eta$ | $A_x$ (MHz) | $A_y$ (MHz) | $A_z$ (MHz) | $\delta$ (mm/s) | $\Delta E_Q$ (mm/s) | $\eta$ | $A_x$ (MHz) | $A_y$ (MHz) | $A_z$ (MHz) | $\delta$ (mm/s) |
| Aae Fd5 | 0.8(1) | −0.4(2) | −56(2) | −50(2) | −42(2) | 0.32(1) | 2.9(1)[b] | 0.4(2) | 24(2) | 13(2) | 35(2) | 0.65(1) |
| Bertrand & Gayda model | | | | | | | + 2.9 | 0.6 | 24.5 | 12.9 | 33.8 | |

[a] The parameters in row 2 were calculated, for $\eta = 0.6$, with the model of Bertrand and Gayda (*44*). The symbols are those used by these authors: $\Theta = -20.4°$ yielding $g_x = 1.926$, $g_y = 1.931$, and $g_z = 2.02$ for $g_{1x} = g_{1y} = 2.020$, $g_{1z} = 2.03$, and $\Delta_{xz} = 8010\ cm^{-1}$, $\Delta_{yz} = 3200\ cm^{-1}$, $\Delta_{xy} = 2000\ cm^{-1}$, and, from Vrajmasu et al. (*45*), $\lambda = -88\ cm^{-1}$ ($\Delta_{xy}$ is quite arbitrary but must be larger that $600\ cm^{-1}$ because $\Delta E_Q$ is independent of temperature up to 230 K); $A_2 = -21.8$ MHz and $P = -55$ MHz (Bertrand and Gayda (*44*) define the internal magnetic field with a sign opposite to that commonly used; we have added a negative sign to $A_2$ and $P$ to adjust the $A$-values of eq 6 (*44*) to the common definition). Numbers in parentheses are uncertainties in the last digits of the values. [b] The largest component of the efg-tensor, $V_{\zeta\zeta}$, is along the $y$ axis; referred to ($x$,$y$,$z$), $\eta = (V_{xx} - V_{zz})/V_{yy} = 0.4$.

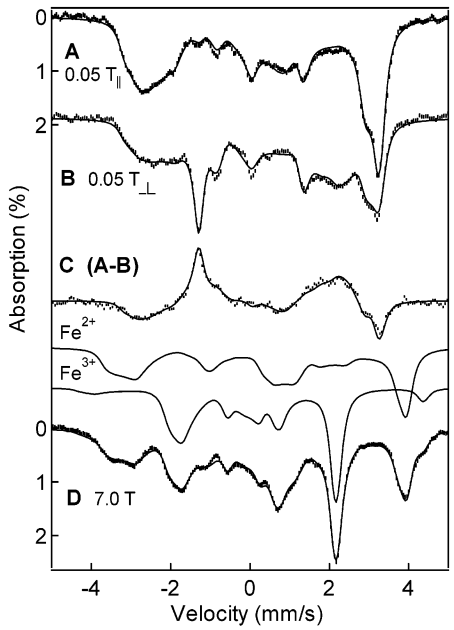


FIGURE 8: 4.2 K Mössbauer spectra of reduced Fd5. (A) 0.05 T parallel field; (B) 0.05 T transverse field; (D) 7.0 T parallel field. 19% of Fd5 was in the oxidized state; this contribution has been removed from the data. The sample contained also a high-spin ferrous contaminant (ca. 4% of Fe); its contribution was removed from spectra A and B. Shown in line (C) is the difference spectrum (A−B); in this procedure the contributions of the ferrous contaminant and oxidized Fd5 cancel. The solid lines are theoretical spectra obtained from eq 1 using the parameters listed in Table 1.

explains with reasonable accuracy the variation of the parameters observed for a large group of ferredoxins. This model considers a rhombically distorted tetrahedral ferrous site with $C_{2v}$ symmetry. The orbital ground state of the ferrous site is described by a mixture of $|z^2\rangle$ and $|x^2 - y^2\rangle$ states

$$|\phi_0\rangle = \cos\Theta\,|z^2\rangle + \sin\Theta\,|x^2 - y^2\rangle \qquad (2)$$

where $\Theta$ is a mixing parameter and the coordinate system is such that $|x^2 - y^2\rangle$ belongs to the $t_{2g}$ set in the limit of tetrahedral symmetry. A recent analysis of reduced rubredoxin by ligand field and density functional theory (*45*) has shown that the electronic ground state is well described by ligand field theory and that the efg-tensor is proportional to the spin-dipolar contribution to the magnetic hyperfine tensor. (This proportionality breaks down for complexes with a substantial ligand contribution to the efg.) Applying similar principles to the ferrous site of Fd5 (see Table 2) provides

Table 2: Contributions to the $A$-Values (MHz) of the Ferrous Site of *Aae* Fd5

| | $A_{total}$ | $A_{spin-dip}$ | $A_{orb}$[a] |
|---|---|---|---|
| $A_x$ | 24.5 | 2.0 | −5.3, −1.2 |
| $A_y$ | 12.9 | −9.9 | −5.3, −0.9 |
| $A_z$ | 33.8 | 7.9 | −5.3, +2.1 |
| $A_{iso}$ | 23.7 | 0 | −5.3 |

[a] The isotropic (left) and anisotropic (right) contributions to $A_{orb}$ have been separated.

an understanding of the hyperfine parameters listed in Table 1. The isotropic contribution to the ferrous **A**-tensor is 23.7 MHz (all values quoted here refer to the coupled representation, i.e., the intrinsic $A$-values of the ferrous site are multiplied by the spin-projection factor −4/3 (*42*)). The anisotropy of the **A**-tensor is mainly due to the spin-dipolar term. The principal component of the efg-tensor of Fd5 is positive and directed along the $y$-axis of the **A**-tensor, implying that the spin-dipolar term decreases the magnitude of $A_y$. For a $|z^2\rangle$ ground state, the largest efg component is negative and along $z$, as observed for the plant-type Fds, and consequently the magnitude of $A_z$ is decreased by the spin dipolar term. Because the efg-tensor of Fd5 is rhombic ($\eta = 0.3-0.6$), the spin-dipolar contribution is rhombic as well, increasing the magnitude of $A_z$ (by about 8 MHz) more than that of $A_x$ (2 MHz increase).

In the Bertrand and Gayda (*44*) model, the asymmetry parameter $\eta$ depends only on the mixing parameter $\Theta$ (eq 5 in ref *44*). Using $\eta = 0.6$ (this choice yields the best match of the model with the data) we obtain $\Theta = -20.4°$. Each of the three principal g-values depends on $\Theta$ and on one of the ligand field parameters $\Delta_{xz}$, $\Delta_{yz}$, and $\Delta_{xy}$. By choosing the $\Delta$-values such that the $g$-values of Fd5 are reproduced, the orbital contribution to the **A**-tensor is obtained (eq 6 in ref *44*). Using this procedure and the ligand field parameters listed in footnote a, the calculated $A$-values listed in Table 1 were obtained.

For Fd5 the ground state of the ferrous site is $|\phi_0\rangle = 0.937|z^2\rangle - 0.349|x^2 - y^2\rangle$. The $|x^2 - y^2\rangle$ admixture moves the major component of the efg from $z$ to $y$. The $z$-axis corresponds to the direction for which the EPR resonance at $g = 2.02$ is observed. It should be noted that the near axial symmetry of the **g**-tensor is accidental as indicated by the observation of rhombic **A**- and efg-tensors; see also Figure 4 of ref *44*.

Table 2 shows the various contributions to the **A**-tensor as calculated with the Bertrand and Gayda model. It can be seen that the spin-dipolar term introduces an 18 MHz

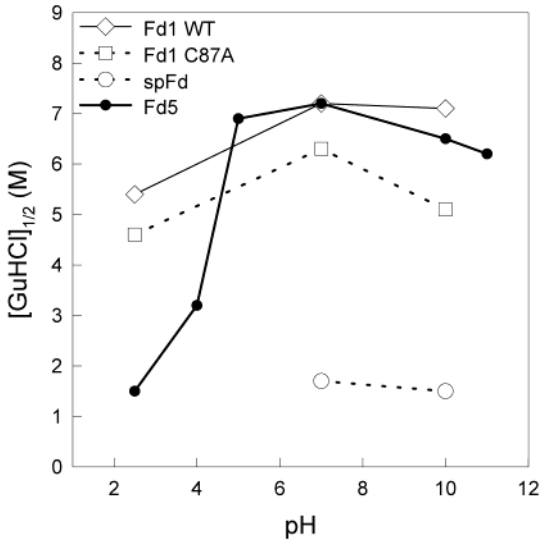


FIGURE 9: Comparison of transition midpoints ($[GuHCl]_{1/2}$) for GuHCl-induced unfolding (20 °C; 12 h incubation) as a function of pH for the various ferredoxins.

anisotropy between $A_y$ and $A_z$, while an additional 3 MHz results from the anisotropic orbital contribution. $A_{iso}(orb) = -5.3$ MHz opposes the Fermi contact term ($A_c = 29$ MHz).

Fixing the parameter Θ by the $\eta$-value of the efg-tensor also works quite well with methane monoxygenase reductase (*43*), for which very good Mössbauer fits have been reported. In contrast, the **A**-tensor of the ferrous site of putidaredoxin is only poorly predicted by the Bertrand and Gayda model. We have therefore attempted to refit the published Mössbauer spectra of that protein (*46*). Unfortunately, the data of 1972 are not readily accessible for processing. Moreover, it is advisable to record data in fields up to 8.0 T for a more accurate determination of $A_x$, $A_y$, and $\eta$. Such studies are under consideration. As a final note, simulating putidaredoxin spectra and overlaying them with the published spectra (*46*) revealed that the ENDOR values for $A_x$ and $A_y$, reported by Sands and Dunham (*47*), are ca. 20% too large and not compatible with the Mössbauer data (the Mössbauer A-values are, however, within the quoted uncertainties of the ENDOR study).

*Redox Potential*. The redox potential of *Aae* Fd5 has been measured by reductive (with dithionite) and oxidative (with ferricyanide) spectrophotometric titration (Materials and Methods). The measured redox potential of −390 ± 10 mV is more within the range of plant-type than of Adx-type proteins (*4*). Significantly, however, it is close to those of the Isc-Fds from *E. coli* (- 380 mV (*48*)) and *A. vinelandii* (−344 mV (*6*)).

*Chemically Induced Unfolding of Aae Fd5*. The native state of *Aae* Fd5, like that of *Aae* Fd1 (*11*), is characterized by negative CD intensity around 210−220 nm due to secondary structure and distinct visible-absorption between 350 and 500 nm due to the oxidized iron−sulfur cluster. *Aae* Fd5 does not have a tryptophan, but it has three tyrosine residues. The tyrosine emission is quenched in the folded state due to energy transfer to the iron−sulfur center (centered around 310 nm). Upon Fd5 unfolding, the far-UV CD signal disappears, the tyrosine emission increases, and the visible absorption diminishes. *Aae* Fd5 is in its native state (as judged by far-UV CD and visible absorption) in solution from pH 1.57 to 12.4 at 20 °C (2 h of incubation). At pH 1.25, the protein is not folded nor is the [2Fe−2S] cluster intact; pH values higher than 12.4 have not been tested.

Table 3: GuHCl-Induced Unfolding Midpoints for *Aae* Fd5, *Aae* Fd1 (WT and C87A), and Spinach Fd at Various pH Values (Probing Technique and Incubation Time as Indicated)

| | | | GuHCl midpoint (M) | | | |
|---|---|---|---|---|---|---|
| pH | probing technique | incubation time (h) | *Aae* Fd1 WT | *Aae* Fd1 C87A | spinach Fd | *Aae* Fd5 |
| 2.5 | Abs (418 nm) | 1 | 6.6 | 6.2 | unfolded | 2 |
| | | 12 | 5.4 | 4.6 | − | 1.5 |
| | Em (365 nm) | 1 | 6.5 | 6.7 | unfolded | 1.9[a] |
| | | 12 | 5.3 | 4.8 | − | 1.4[a] |
| | CD (220 nm) | 12 | 5 | 4.4 | unfolded | 1.5 |
| 4 | Abs (418 nm) | 12 | − | − | − | 3.2 |
| | Em (310 nm) | 12 | − | − | − | 3.2[a] |
| | CD (220 nm) | 12 | − | − | − | 3.1 |
| 5 | Abs (418 nm) | 12 | − | − | − | 6.7 |
| | Em (310 nm) | 12 | − | − | − | 6.9[a] |
| | CD (220 nm) | 12 | − | − | − | 6.7 |
| 7 | Abs (418 nm) | 2 | no unfolding | 6.5 | 2.1 | 7.6 |
| | | 12 | 7.2 | 6.3 | 1.7 | 7.4 |
| | | 24 | 6.7 | 6.1 | 1.5 | 7.0 |
| | | 48 | − | − | − | 6.8 |
| | Em (365 nm) | 2 | − | − | − | 7.6[a] |
| | | 12 | − | − | − | 7.1[a] |
| | | 24 | 6.4 | 6.2 | 1.6 | 7[a] |
| | | 48 | − | − | − | 6.9[a] |
| | CD (220 nm) | 2 | − | 6.8 | 2.1 | 7.6 |
| | | 12 | 7.2 | 6.2 | − | 7.0 |
| | | 24 | 6.4 | − | 1.6 | 6.9 |
| | | 48 | − | − | − | 6.8 |
| 10 | Abs (418 nm) | 1 | 7.5 | 5.2 | 3.0 | [b] |
| | | 12 | 7.1 | 5.1 | 1.5 | [b] |
| | | 24 | − | − | − | [b] |
| | Em (365 nm) | 12 | 7.0 | 5.1 | 1.6 | 6.5[a] |
| | | 48 | − | − | − | 6.1[a] |
| | CD (225 nm) | 12 | 7.0 | 5.3 | 1.6 | 6.6 |
| | | 24 | − | − | − | 6.3 |
| | | 48 | − | − | − | 6.1 |
| 11 | Abs (418 nm) | 12 | − | − | − | [b] |
| | Em (310 nm) | 12 | − | − | − | 6.2[a] |
| | CD (235 nm) | 12 | − | − | − | 6.2 |

[a] Emission monitored at 310 nm. [b] Intermediate with new absorption bands forms; therefore, unfolding midpoints are not reliable by this technique.

GuHCl-induced Fd5 unfolding at 20 °C is irreversible, as in the case of *Aae* Fd1 (*11*, *49*). The unfolding data are therefore described in terms of transition midpoints for various incubation times (Table 3, Figure 9). The transition midpoints observed by the different spectroscopic probes at identical incubation times roughly agree with each other (Table 3), suggesting that Fd5 unfolding is an apparent two-state process without populated intermediates. At pH 7 and above, Fd5 is highly resistant toward chemical perturbation. Very high concentrations of GuHCl and long incubation times are required to promote unfolding. The stability of Fd5 at neutral or alkaline pH is similar to that of WT and C87A *Aae* Fd1, but it is significantly less stable than the latter at pH 2.5 (Table 3, Figure 9). In fact, the unfolding midpoints for Fd5 at pH 2.5 are similar to those of the mesophilic spinach Fd at pH 7 and 10.

*Thermally Induced Unfolding of Fd5*. Thermal unfolding of Fd5 is also irreversible. The influence of the irreversible steps was eliminated by extrapolating values for thermal midpoints ($T_m$) at various scan rates to infinite scan rate. Thermal unfolding of Fd5 shows a similar pH trend as that

Table 4: pH Dependence of Thermally induced Unfolding Midpoints for the Reversible Step of *Aae* Fd5, *Aae* Fd1 (WT and C87A), and Spinach Fd[a]

| | $T_m$ at infinite scan rate (°C) | | | |
|---|---|---|---|---|
| pH | *Aae* Fd1 WT | *Aae* Fd1 C87A | spinach Fd | *Aae* Fd5 |
| 7 | 121 | 113 | 70 | 106 |
| 2.5 | 79 | 68 | - | 55 |
| 10 | 116 | 105 | 53 | 102 |

[a] See text for details.

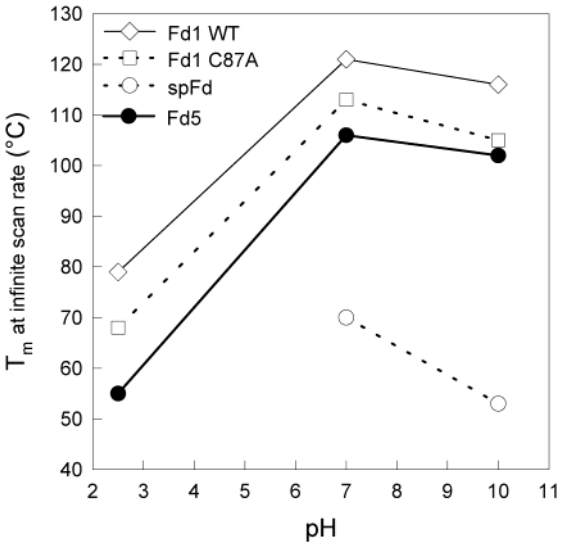


FIGURE 10: Comparison of thermal midpoints (infinite scan rate) as a function of pH for the various ferredoxins.

found in the chemical-denaturant studies. At pH 7 and 10, Fd5 is very stable and exhibits similar $T_m$ values as Fd1 and C87A Fd1 (although slightly lower). At pH 2.5, in contrast, Fd5 is significantly less stable than Fd1 and C87A Fd1 (Table 4, Figure 10).

*Interaction with Hydrogenase*. Regardless of their cellular function, a number of plant- and mammalian-type [2Fe−2S] Fds have been found to be efficient redox partners of some hydrogenases. Reversible electron transfer between an [Fe] hydrogenase from *C. pasteurianum* and a variety of plant- and algal Fds has been described repeatedly (*50*−*53*). *Aae* Fd5 belongs to the large family of plant- and mammalian-type Fds, and its redox potential, at − 390 mV, is close to the potential of the hydrogen electrode. It could therefore be anticipated to operate as an efficient and very stable electron donor to hydrogenase. Contrary to that expectation, however, *Aae* Fd5 and, likewise, *Aae* Fd1 were found to function neither as electron donors (for $H_2$ evolution) nor as electron acceptors (for $H_2$ oxidation) with *C. pasteurianum* [Fe] hydrogenase. This observation reveals that the latter hydrogenase interacts less promiscuously with [2Fe−2S] Fds, even low-potential ones, than inferred from previous observations (*53*).

*Putative Function of A. aeolicus Fd5*. The properties of *Aae* Fd5 relate it to Isc-Fds, as indicated by the primary structure (Figure 2), spectroscopic signatures (Figures 3−6), and relatively low redox potential. This suggests that *Aae* Fd5 might be the Isc-Fd from *A. aeolicus*. On the other hand, the Fd5-encoding gene is most likely monocistronic (Figure 1), in contrast to the situation encountered in most other bacteria where the Isc-Fd-encoding genes belong to the *isc* operon committed to iron−sulfur cluster assembly (*54*, *55*). It should nevertheless be noted that in *A. aeolicus isc*-like genes, and likewise genes committed to other functions (*15*, *53*), are scattered throughout the genome rather than clustered in one operon. The genomic context is therefore of little use for functional inferences. While Fd5 is most likely the Isc-Fd of *A. aeolicus*, conclusive evidence nevertheless remains to be obtained by biochemical and genetic studies.

## CONCLUSIONS

Prior to this report, a single hyperthermophilic plant- and mammalian-type [2Fe−2S] Fd had been characterized, namely Fd1 from *A. aeolicus* (*11*). We have subsequently found in the genome of *A. aeolicus* a heretofore undetected gene encoding another Fd of that type. The latter gene has been overexpressed in *E. coli* and its product (Fd5) has been characterized. Rather surprisingly, systematic searches of available genomes from hyperthermophiles have failed to reveal other genes potentially encoding [2Fe−2S] plant- and mammalian-type Fds. Such a void in an otherwise very widely distributed family of proteins constitutes an anomaly. It appears not to be ascribable to an intrinsic instability of these Fds (see below) and is therefore most likely the result of phylogenetic events that remain to be analyzed.

Fd5 from *A. aeolicus* is very thermostable, as illustrated by its thermal denaturation midpoint (106 °C), which is well above 100 °C. This protein nonetheless lacks some characteristic features usually associated with hyperthermostability, in particular a high content of glutamate and lysine residues (*27*). This observation is consistent with the relatively high stability of many mesophilic plant-type Fds (*3*, see also Tables 3 and 4) and suggests that such proteins can be shifted into the realm of hyperthermophily by moderate sequence alterations. Indeed, *Aae* Fd1, which is endowed with a high content of glutamate and lysine and is in addition stabilized by a disulfide bridge, is even more stable ($T_m$ = 121 °C) than *Aae* Fd5 (*11*, *49*). These data show that there are no thermodynamic barriers disfavoring the presence of plant-type Fds in hyperthermophiles.

Although the function of *Aae* Fd5 has not been established experimentally, the primary structure as well as EPR, Resonance Raman, and MCD data all point to a high similarity with bacterial Fds that are involved in Fe−S cluster biosynthesis (Isc-Fd). Mössbauer data could not be used for comparisons, as this technique has not yet been applied to Isc-Fds. *Aae* Fd5 nevertheless possesses a few idiosyncrasies which set it somewhat aside of bona fide Isc-Fds. For instance, it has shorter N- and C-termini, and is devoid of cysteine residues other than the Fe−S cluster ligands. This suggests that experiments aimed at establishing whether *Aae* Fd5 is indeed an Isc-Fd may bring forth valuable information regarding functionally relevant features of this group of proteins. It is also worth noting that *Aae* Fd5 appears to be encoded by a monocistronic gene while Isc-Fd-encoding genes are most often part of *isc* operons. However, this is not an exceptional occurrence in the genome of *A. aeolicus*: for instance, genes encoding subunits of complex I, as well as hydrogenase chaperones, are scattered over several loci (*15*), whereas in most bacteria they are assembled in operons. This peculiarity of the *A. aeolicus* genome remains to be fully assessed and analyzed.

Regardless of the yet to be established function of *Aae* Fd5, the spectroscopic data reported here (which include spectra of *A. vinelandii* Isc-Fd) are of interest in two respects. First, these are the first resonance Raman and VTMCD spectra, and perhaps Mössbauer spectra as well if Fd5 turns out to be an Isc-Fd, reported for any Isc-Fd. Second, we have extended the analysis of the $[2Fe-2S]^{+}$ Mössbauer spectra in the framework of the Bertrand and Gayda model (*44*), pointing out the usefulness of the asymmetry parameter $\eta$ as a point of departure for the ligand field analysis. A recent structural correlation analysis of rubredoxin (*45*) suggests that $\eta$ is highly correlated with the spin-dipolar contribution of the magnetic hyperfine tensor. While this needs to be further explored, it should be noted that $\eta$ is generally very difficult to determine, primarily because it can be traded against two A-tensor components in the spin Hamiltonian fits (see Figure 18 in ref *43*). Therefore, it would be very useful to conduct for some ferredoxins $^{57}$Fe ENDOR studies at Q-band. This would move $^{1}$H resonances away from the spectral region where they interfere with the $^{57}$Fe signals and would thus allow a direct assessment of the *A*-values of the ferrous site.

The isolation and characterization of *Aae* Fd5 has significantly extended the known distribution of plant- and mammalian-type Fds, and at the same time highlighted domains of life from which they surprisingly appear to be absent. *Aae* Fd5 may also be expected to shed light on structure/function relationships within the group of Isc-Fd. Finally, *Aae* Fd5 and *Aae* Fd1 are targets of opportunity to study the structural parameters ruling protein thermostability.

## ACKNOWLEDGMENT

We thank Jean-Pierre Andrieu and Jean Gagnon (IBS, Grenoble) for N-terminal sequences and amino acid analyses, and Myriam Ferro (DBMS, CEA-Grenoble) for mass spectra. We thank Dennis R. Dean for supplying the strain of *E. coli* containing the plasmid for overexpression of *Av* Isc-Fd.

## SUPPORTING INFORMATION AVAILABLE

Figures showing the sequence alignment wherefrom the dendrogram of Figure 2 was derived, as well as sequence alignments of Isc-Fds. This material is available free of charge via the Internet at http://pubs.acs.org.

## REFERENCES

1. Beinert, H., Holm, R. H., and Münck, E. (1997) *Science 277*, 653−659.
2. Johnson, M. K. (1994) in *Encyclopedia of Inorganic Chemistry* (King, R. B., Ed.) Vol. 4 pp 1896−1915, Wiley, Chichester, U.K.
3. Matsubara, H., and Saeki, K. (1992) *Adv. Inorg. Chem. 38*, 223−280.
4. Grinberg, A. V., Hannemann, F., Schiffler, B., Müller, J., Heinemann, U., and Bernhardt, R. (2000) *Proteins 40*, 590−612.
5. Meyer, J. (2001) *FEBS Lett. 509*, 1−5.
6. Jung, Y.-S., Gao-Sheridan, H. S., Christiansen, J., Dean, D. R., and Burgess, B. K. (1999) *J. Biol. Chem. 274*, 32402−32410.
7. Lange, H., Kaut, A., Kispal, G., and Lill, R. (2000) *Proc. Natl. Acad. Sci. U.S.A. 97*, 1050−1055.
8. Tokumoto, U., and Takahashi, Y. (2001) *J. Biochem. 130*, 63−71.
9. Barros, M. H., and Nobrega, F. G. (1999) *Gene 233*, 197−203.
10. Hugo, N., Armengaud, J., Gaillard, J., Timmis, K. N., and Jouanneau, Y. (1998) *J. Biol. Chem. 273*, 9622−9629.
11. Meyer, J., Clay, M. D., Johnson, M. K., Stubna, A., Münck, E., Higgins, C., and Wittung-Stafshede, P. (2002) *Biochemistry 41*, 3096−3108.
12. Bertini, I., Luchinat, C., Provenzani, A., Rosato, A., and Vasos, P. R. (2002) *Proteins 46*, 110−127.
13. Yoo, S.-J., Meyer, J., and Münck, E. (1999) *J. Am. Chem. Soc. 121*, 10450−10451.
14. Ausubel, F. M., Brent, R., Kingston, R. E., Moore, D. D., Seidman, J. G., Smith, J. A., and Struhl, K. (2001) *Current Protocols in Molecular Biology*, Wiley-Interscience, New York.
15. Deckert, G., Warren, P. V., Gaasterland, T., Young, W. G., Lenox, A. L., Graham, D. E., Overbeek, R., Snead, M. A., Keller, M., Aujay, M., Huber, R., Feldman, R. A., Short, J. M., Olsen, G. J., and Swanson, R. V. (1998) *Nature 392*, 353−358.
16. Tabor, S. (1990) in *Current Protocols in Molecular Biology* (Ausubel, F. M., Brent, R., Kingston, R. E., Moore, D. D., Seidman, J. G., Smith, J. A., and Struhl, K., Eds.) p 16.2.1−16.2.11, Wiley-Interscience, New York.
17. Fujinaga, J., and Meyer, J. (1993) *Biochem. Biophys. Res. Commun. 192*, 1115−1122.
18. Meyer, J., Gagnon, J., Gaillard, J., Lutz, M., Achim, C., Münck, E., Pétillot, Y., Colangelo, C. M., and Scott, R. A. (1997) *Biochemistry 36*, 13374−13380.
19. Beinert, H. (1978) *Methods Enzymol. 54*, 435−445.
20. Quinkal, I., Davasse, V., Gaillard, J., and Moulis, J.-M. (1994) *Protein Eng. 7*, 681−687.
21. Golinelli, M.-P., Akin, L. A., Crouse, B. R., Johnson, M. K., and Meyer, J. (1996) *Biochemistry 35*, 8995−9002.
22. Johnson, M. K. (1988) in *Metal Clusters in Proteins* (Que, L., Jr., Ed.) ACS Symposium Series, Vol. 372, pp 326−342, American Chemical Society, Washington, DC.
23. Thomson, A. J., Cheesman, M. R., and George, S. J. (1993) *Methods Enzymol. 226*, 199−232.
24. Drozdzewski, P. M., and Johnson, M. K. (1988) *Appl. Spectrosc. 42*, 1575−1577.
25. Altschul, S. F., Madden, T. L., Schäffer, A. A., Zhang, J., Zhang, Z., Miller, W., and Lipman, D. J. (1997) *Nucleic Acids Res. 25*, 3389−3402.
26. Chatelet, C., Gaillard, J., Pétillot, Y., Louwagie, M., and Meyer, J. (1999) *Biochem. Biophys. Res. Commun. 261*, 885−889.
27. Cambillau, C., and Claverie, J.-M. (2000) *J. Biol. Chem. 275*, 32383−32386.
28. Crossnoe, C. R., Germanas, J. P., LeMagueres, P., Mustata, G., and Krause, K. L. (2002) *J. Mol. Biol. 318*, 503−518.
29. Thompson, J. D., Higgins, D. G., and Gibson, T. J. (1994) *Nucleic Acids Res. 22*, 4673−4680.
30. Page, R. D. M. (1996) *Comput. Appl. Biosci. 12*, 357−358.
31. Ta, D. T., and Vickery, L. E. (1992) *J. Biol. Chem. 267*, 11120−11125.
32. Meyer, J., Moulis, J.-M., and Lutz, M. (1986) *Biochim. Biophys. Acta 873*, 108−118.
33. Han, S., Czernuszewicz, R. S., and Spiro, T. G. (1989) *J. Am. Chem. Soc. 111*, 349−3504.
34. Han, S., Czernuszewicz, R. S., Kimura, T., Adams, M. W. W., and Spiro, T. G. (1989) *J. Am. Chem. Soc. 111*, 3505−3511.
35. Fu, W., Drozdzewski, P. M., Davies, M. D., Sligar, S. G., and Johnson, M. K. (1992) *J. Biol. Chem. 267*, 15502−15510.
36. Gibson, J. F., Hall, D. O., Thornley, J. H. M., and Whatley, F. R. (1966) *Proc. Natl. Acad. Sci. U.S.A.* 56, 987−990.
37. Bertrand, P., Guigliarelli, B., Gayda, J.-P., Beardwood, P., and Gibson, J. F. (1985) *Biochim. Biophys. Acta 831*, 261−266.
38. Werth, M. T., Cecchini, G., Manodori, A., Ackrell, B. A. C., Schröder, I., Gunsalus, R. P., and Johnson, M. K. (1990) *Proc. Natl. Acad. Sci. U.S.A. 87*, 8965−8969.
39. Thomson, A. J., Cammack, R., Hall, D. O., Rao, K. K., Briat, B., Rivoal, J. C., and Badoz, J. (1977) *Biochim. Biophys. Acta 493*, 132−141.
40. Tsibris, J. C. M., Tsai, R. L., Gunsalus, I. C., Orme-Johnson, W. H., Hansen, R. E., and Beinert, H. (1968) *Proc. Natl. Acad. Sci. U.S.A. 59*, 959−965.
41. Mukai, K., Kimura, T., Helbert, J., and Kevan, L. (1973) *Biochim. Biophys. Acta 295*, 49−61.
42. Münck, E. (2000) in *Physical Methods in Bioinorganic Chemistry Spectroscopy and Magnetism* (Que, L., Jr., Ed.) pp 287−319, University Science Books, Sausalito, CA.
43. Fox, B. G., Hendrich, M. P., Surerus, K. K., Andersson, K. K., Foland, W. A., Lipscomb, J. D., and Münck, E. (1993) *J. Am. Chem. Soc. 115*, 3688−3701.

44. Bertrand, P., and Gayda, J.-P. (1979) *Biochim. Biophys. Acta 579*, 107−121.
45. Vrajmasu, V. V., Bominaar, E. L., Meyer, J., and Münck, E. (2002) *Inorg. Chem. 41*, 6358−6371.
46. Münck, E., Debrunner, P. G., Tsibris, J. C. M., and Gunsalus, I. C. (1972) *Biochemistry 11*, 855−863.
47. Sands, R. H., and Dunham, R. W. (1975) *Quart. Rev. Biophys. 7*, 443−504.
48. Knoell, H.-E., and Knappe, J. (1974) *Eur. J. Biochem. 50*, 245−252.
49. Higgins, C., Meyer, J., and Wittung-Stafshede, P. (2002) *Biochim. Biophys. Acta 1599*, 82−89.
50. Tagawa, K., and Arnon, D. I. (1962) *Nature 195*, 537−543.
51. Fitzgerald, M. P., Rogers, L. J., Rao, K. K., and Hall, D. O. (1980) *Biochem. J. 192*, 665−672.
52. Moulis, J.-M., and Davasse, V. (1995) *Biochemistry 34*, 16781−16788.
53. Vignais, P. M., Billoud, B., and Meyer, J. (2001) *FEMS Microbiol. Rev. 25*, 455−501.
54. Frazzon, J., and Dean, D. R. (2001) *Proc. Natl. Acad. Sci. U.S.A. 98*, 14751−14753.
55. Tokumoto, U., Nomura, S., Minami, Y., Mihara, H., Kato, S.-I., Kurihara, T., Esaki, N., Kanazawa, H., Matsubara, H., and Takahashi, Y. (2002) *J. Biochem. 131*, 713−719.

BI027116N